Earth and Planetary Science Letters 622 (2023) 118404

Contents lists available at ScienceDirect

Earth and Planetary Science Letters

journal homepage: www.elsevier.com/locate/epsl

Spatially heterogenous seawater $\delta^{34}S$ and global cessation of Ca-sulfate burial during the Toarcian oceanic anoxic event

Zhong Han [a,b], Xiumian Hu [b,*], Robert J. Newton [c], Tianchen He [c], Benjamin J.W. Mills [c], Hugh C. Jenkyns [d], Micha Ruhl [e], Robert A. Jamieson [c]

[a] State Key Laboratory of Oil and Gas Reservoir Geology and Exploitation and Key Laboratory of Deep-time Geography and Environment Reconstruction and Applications, MNR, Institute of Sedimentary Geology, Chengdu University of Technology, Chengdu 610059, China
[b] State Key Laboratory of Mineral Deposit Research, School of Earth Sciences and Engineering, Nanjing University, Nanjing 210023, China
[c] Earth Surface Science Institute, School of Earth and Environment, University of Leeds, Woodhouse Lane, Leeds LS2 9JT, UK
[d] Department of Earth Sciences, University of Oxford, South Parks Road, Oxford OX1 3AN, UK
[e] Department of Geology, Trinity College Dublin, The University of Dublin, Dublin, Ireland

ARTICLE INFO

Article history:
Received 12 April 2023
Received in revised form 2 August 2023
Accepted 12 September 2023
Available online xxxx
Editor: A. Jacobson

Keywords:
Toarcian Oceanic Anoxic Event
CAS sulfur isotopes
heterogenous $\delta^{34}S$ ocean
stepwise deoxygenation
negligible Ca-sulfate deposition

ABSTRACT

The early Toarcian of the Early Jurassic saw a long-term positive carbon-isotope excursion (CIE) abruptly interrupted by a significant negative excursion (*n*CIE), associated with rapid global warming and an oceanic anoxic event (T-OAE, ~183 Ma). However, the detailed processes and mechanisms behind widespread ocean deoxygenation are unclear. Here, we present high-resolution carbonate-associated sulfate sulfur-isotope ($\delta^{34}S_{CAS}$) records spanning the late Pliensbachian–Toarcian (Pl–To) interval from the Tibetan Himalaya. We observe a large positive sulfur-isotope excursion (SIE) from ~20‰ (around the Pl–To boundary) to ~40‰ (around the end of the T-OAE *n*CIE), attributed to large-scale burial of reduced sulfur (pyrite and sulfurized organic matter) under widespread anoxic/euxinic conditions. Importantly, high $\delta^{34}S_{CAS}$ values were maintained into the mid–late Toarcian, even when global anoxic conditions diminished. The $\delta^{34}S$ data confirm significant spatial heterogeneity in seawater $\delta^{34}S$ compositions during the whole of the Toarcian, and provide strong evidence for a two-phase pattern of ocean deoxygenation. Upwelling of ^{34}S-enriched equatorial deep water, affected by significant reduced-sulfur burial, likely caused the greatly amplified SIE in the formerly adjacent Tibetan area. By contrast, the dampened magnitude of the Toarcian SIE in Europe is attributed to a smaller, local reduced-sulfur sink. Box-modeling results indicate that the persistent post-T-OAE positive $\delta^{34}S$ values were likely maintained because of a global reduction in Ca-sulfate (gypsum and anhydrite) burial driven by declining and continuously low seawater sulfate concentrations during and after the T-OAE. This geochemical pattern, albeit markedly reducing the total amount of global pyrite sequestration, increased the proportion of reduced to oxidized sulfur burial needed to generate the observed positive $\delta^{34}S$ values.

1. Introduction

Episodes of rapid global warming, known as hyperthermals, have punctuated Earth history and are typically associated with the expansion and intensification of oxygen-depleted waters in the world ocean. Such events in the Mesozoic, termed Oceanic Anoxic Events (OAEs), have been recognized and well documented in the early Toarcian, early Aptian and at the Cenomanian–Turonian boundary (e.g., Jenkyns, 2010; Hu et al., 2020). Although the OAE concept was introduced in the nineteen-seventies based on the coeval occurrence of black shales worldwide and the associated typical positive carbon-isotope signatures (Jenkyns, 2010), understanding of the processes and mechanisms behind deoxygenation remains incomplete.

The Toarcian OAE (T-OAE) of the Early Jurassic is one of the most widely recognized examples of this phenomenon because of the global distribution of coeval organic-rich black shales from both epicontinental and pelagic settings across both hemispheres (Jenkyns, 1988, 2010; Kemp et al., 2022a). In stratigraphically complete sequences, the T-OAE is characterized by an overarching positive carbon-isotope excursion (T-OAE *p*CIE) incised by an abrupt and stepped negative excursion (*n*CIE; Fig. 1A), the latter conventionally linked to the introduction of ^{13}C-depleted carbon from the Karoo-Ferrar Large Igneous Provinces (LIPs), thermogenic methane

* Corresponding author.
E-mail address: huxm@nju.edu.cn (X. Hu).

https://doi.org/10.1016/j.epsl.2023.118404
0012-821X/

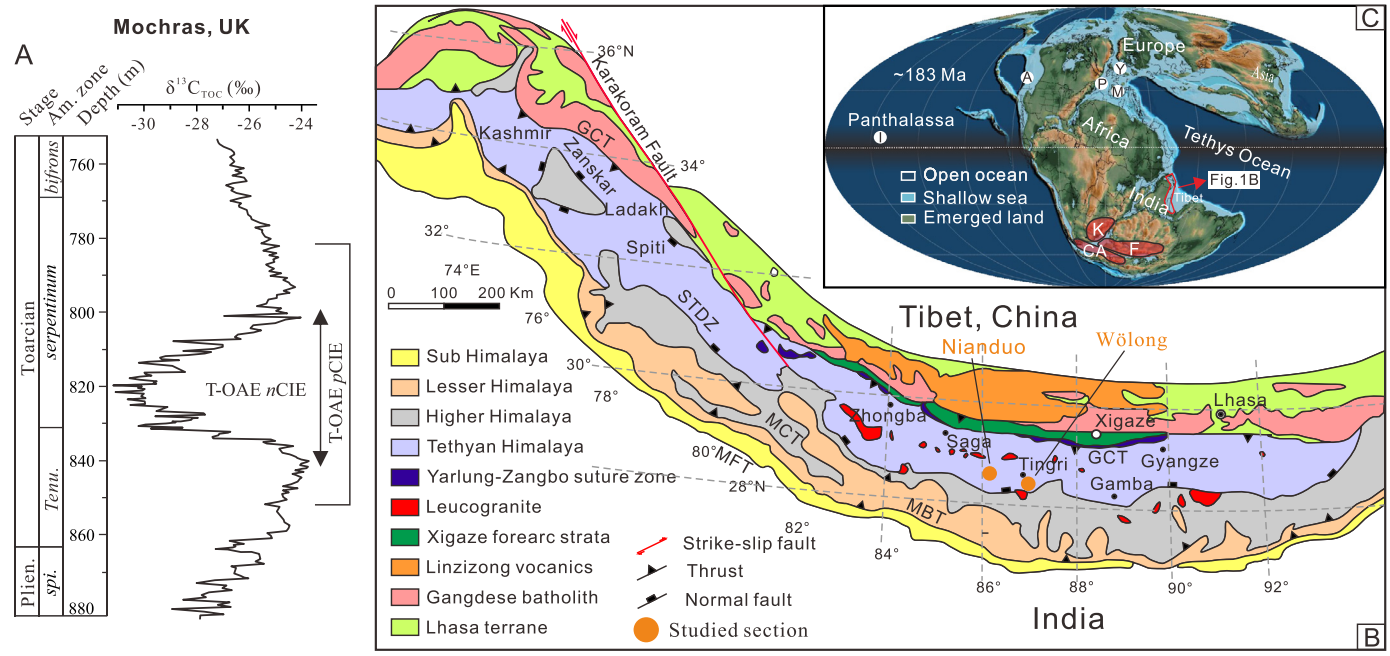

Fig. 1. Toarcian characteristic carbon-isotope stratigraphy and global palaeogeography and geological sketch map of the Himalaya. **A.** Uppermost Pliensbachian–Lower Toarcian carbon-isotope stratigraphy is from the Mochras borehole (Wales, UK) with a complete succession and well-constrained ammonite biostratigraphy (Xu et al., 2018a). Note that the onset of the classic T-OAE pCIE pre-dates the nCIE, which has been mistaken for the OAE. **B.** Geological setting of the Himalaya showing the two studied sections, modified after Hu et al. (2016). **C.** Palaeogeographic map, showing the studied area and key locations, is adapted from Scotese (2021). The black shaded band represents the equatorial high-productivity zone tentatively identified as the major carbon and reduced-sulfur sink during the T-OAE. Abbreviations: A-Alberta, Canada; Y-Yorkshire, P-Peniche, Portugal; M-Monte Sorgenza, Apennine Carbonate Platform; I-Inuyama, Japan; Am. zone = Ammonite zone; Plien. = Pliensbachian; Toar. = Toarcian; Spi. = Spinatum; Tenu. = Tenuicostatum.

and/or methane hydrate dissociation (Hesselbo et al., 2000; Kemp et al., 2005; Jenkyns, 2010; Burgess et al., 2015; Xu et al., 2018a). Large-scale carbon injection from multiple sources into the global ocean–atmosphere system would have driven rapid global warming, ocean acidification, enhanced continental weathering and associated nutrient input and accelerated primary productivity in the oceans (Jenkyns, 2010; Percival et al., 2016; Kemp et al., 2020; Müller et al., 2020). These phenomena represent important feedback mechanisms reducing atmospheric CO_2 and thereby potentially sowing the seeds of climatic recovery, offsetting the effects of greenhouse-gas introduction from volcanic and other processes.

Organic-carbon burial and sequestration has been widely observed in northern Europe (Jenkyns, 2010), and locally in Japan, and in the Koryak Highland and Kamchatka Peninsula of eastern Russia, in exotic terrains representing deep-sea environments below the carbonate compensation depth (CCD) during the T-OAE (Jenkyns, 1988; Gröcke et al., 2011; Ikeda et al., 2018; Filatova et al., 2022). However, organic-rich sediments are more limited over the entire southern Tethyan margin (e.g., Jenkyns and Clayton, 1986; Hesselbo et al., 2007; Jenkyns, 2010; Trecalli et al., 2012; Han et al., 2018) as well as in some basins in marginal areas of Panthalassa (western North and South America and Japan (Caruthers et al., 2011; Fantasia et al., 2018; Kemp et al., 2022a). Furthermore, coeval redox proxies are spatially heterogeneous because they were typically influenced by local as well as global factors (McArthur et al., 2008). Notably, evidence from thallium isotopes (ε^{205}Tl) from Europe and Canada, and global patterns of organic-matter burial, indicate that widespread deoxygenation began around the Pliensbachian–Toarcian (Pl–To) boundary time and underwent a second pulse coincident with the recovery interval the T-OAE *n*CIE, with the development of expanded oxygen minima likely continuing into the latest early and middle Toarcian (post-*n*CIE; Them et al., 2018; Silva et al., 2021). The relationship between the carbon-cycle perturbations and deoxygenation processes, and their terminations, are therefore poorly constrained for the T-OAE.

The biochemical sulfur cycle plays a key role in regulating the Earth's surface redox state via the metabolic activities of sulfate reduction, disproportionation, and sulfide oxidation: processes that are intimately associated with the global carbon cycle and climatic and environmental change (e.g., Garrels and Lerman, 1981). Examination of the ancient sulfur cycle thus offers an effective way to trace oceanic redox conditions and associated climatic and environmental changes. The few previous studies on the Toarcian sulfur cycle were based on localities in northern Europe and the western and eastern Tethys in an attempt to explore the extent of oceanic anoxia/euxinia and seawater sulfate concentrations using sulfur isotopes ($\delta^{34}S_{CAS}$) in carbonate-associated sulfate (Gill et al., 2011a; Newton et al., 2011). However, there are still uncertainties on the veracity of data from the Tibetan Kioto Platform because of the extremely high $\delta^{34}S_{CAS}$ values compared with those from European sections (Gill et al., 2011a). Here, we present high-resolution $\delta^{34}S_{CAS}$ data from two Tibetan carbonate-platform sections (Wölong and Nianduo), previously investigated by Han et al. (2016, 2018, 2021, 2022a, 2022b), to constrain the dynamics of the sulfur cycle and the implications for detailed reconstructions of oceanic environmental changes in the Toarcian.

2. Geological setting and stratigraphy

The study sites are located in the Tethys Himalaya, bordered by the Yarlung Zangbo Suture Zone to the north and the Greater Himalaya to the south (Fig. 1B). During the Jurassic, the Tethys Himalaya was located on the northern margin of the Indian continent at low southern latitudes (21.8°S to 26.1°S) in the southeastern Neotethys (Fig. 1C; Huang et al., 2015). Over that time interval, the Tethys Himalaya was a mature passive margin that was characterized by deep-water silty shales, calcareous shales, and marls in the northern zone and by shallow-water siliciclastics and carbonates in

the southern zone (Liu and Einsele, 1994; Jadoul et al., 1998; Han et al., 2016).

Carbonate deposits on the so-called Kioto Platform were extensively developed during the Pliensbachian to Toarcian interval in the southern zone of the Tethys Himalaya. This interval has been well studied in the Nianduo and Wölong sections, and has been traditionally subdivided into two units, from the bottom to top: the Pupuga and Nieniexiongla Formations (Jadoul et al., 1998; Han et al., 2016, 2022a, 2022b). The Pupuga Formation is dominated by bioclastic grainstones/packstones laid down on a shallow-water carbonate platform. The overlying lower Nieniexiongla Formation is characterized by finer-grained micrites alternating with common coarser grained storm-generated beds, whereas the upper member of the Nieniexiongla Formation is characterized by more common siltstone (Jadoul et al., 1998; Han et al., 2016, 2018). The Pupuga Formation is dated as Pliensbachian to lowest Toarcian based on the biostratigraphy of *Lithiotis* bivalves, larger benthic foraminifera and carbon-isotope chemostratigraphy (Han et al., 2018, 2021). In particular, the T-OAE has been placed at the Pupuga–Nieniexiongla transitional interval, suggested by the occurrence of the characteristic negative CIE, evidence for significant sea-level rise, carbonate-platform crisis, and common storm-generated layers (Han et al., 2016, 2021). Additionally, the upper member of the Nieniexiongla Formation was inferred to be Bajocian in age from ammonite biostratigraphy (Jadoul et al., 1998). Consequently, if complete, the lower Nieniexiongla Formation should encompass the Toarcian and probably part of the Aalenian.

3. Materials and methods

3.1. CAS and reduced-sulfur extraction

Samples in this study were collected from the upper Pupuga Formation from both sections. At Nianduo, the whole of the lower Nieniexiongla Formation was sampled, whilst at Wölong sampling only took place up to the lower part of the lower Nieniexiongla Formation. Weathered surfaces and crusts were removed from hand samples before powdering using a mechanical agate disc mill. A modified and miniaturized procedure developed by He et al. (2019) was applied to extract carbonate-associated sulfate (CAS) from these samples. Approximately 6–8 g of powdered bulk carbonate was bleached in an excess of 5% NaOCl solution for 72 h to fully oxidize the reduced-sulfur phases, including sulfide minerals and organic sulfur, into sulfate. After filtration through 0.25 μm Polypropylene membrane syringe filters, 6 M HCl was added to the bleached solution to decrease the pH, followed by addition of supersaturated $BaCl_2$ solution to precipitate $BaSO_4$ over at least one week. The solid residue of each sample was washed three times using ultrapure water (18.2 MΩ.cm), and then immersed in 10% (wt/vol) NaCl solution for 24 h with constant agitation. This H_2O-NaCl rinsing step was repeated five times to fully remove the soluble sulfate from the oxidation of reduced-sulfur compounds caused by the NaOCl rinsing step. After these steps, an additional five rinses of the bleached solid residues with ultrapure water were carried out to completely remove residual soluble sulfate and NaCl. No $BaSO_4$ precipitation was observed to have formed by adding $BaCl_2$ to the final rinse filtrate. The leached solid residue of each sample was treated with an excess of 6 M HCl to release the CAS in the carbonate lattice; this was subsequently centrifuged and filtered immediately to minimize the possibility of oxidation of surviving reduced sulfur during carbonate dissolution. The acidified samples were filtered to separate the solid residues and solution. To the latter, 2 ml supersaturated $BaCl_2$ was added to precipitate $BaSO_4$. The resulting NaOCl- and CAS-$BaSO_4$ precipitates of each sample were washed and centrifuged repeatedly until the pH reached neutral values, and were finally extracted, dried and then weighed for sulfur-isotope determination.

3.2. Sulfur-isotope and elemental concentration measurement

Sulfur-isotope analysis was performed on an Elementar vario PYRO cube coupled to a GV Isoprime mass spectrometer in continuous flow mode at the University of Leeds. Dried $BaSO_4$ powders (0.130–0.220 mg) were weighed into tin cups, and flash-combusted into SO_2 in the presence of excess pure O_2 at 1050 °C. Excess O_2 from the gas stream was consumed by reaction with pure copper wire at 850 °C, and water was removed using a Sicapent trap. The resulting SO_2 was separated from other gases by a temperature-controlled trap and purge column. The $\delta^{34}S$ value was obtained using the integrated mass 64 and 66 signals from the SO_2 pulse relative to those in a reference gas. These results were calibrated to the international Vienna-Canyon Diablo Troilite (V-CDT) standard using a chalcopyrite inter-laboratory standard (CP-1) and a seawater-derived laboratory standard (SWS-3), with assigned values of −4.56‰ and +20.3‰ respectively. These laboratory standards were calibrated using the following international reference standards (assigned values in brackets): NBS-123 (17.01‰), NBS-127 (20.3‰), IAEA S-1 (−0.30‰) and IAEA S-3 (−32.06‰). The precision, based on repeated analysis of a laboratory barium sulfate check standard, was ±0.3‰ (1 SD) or better.

An aliquot of the HCl-leachate solution, taken before adding $BaCl_2$, was retained to analyze the concentration of sulfur and metal elements (Ca, Mg, Mn, and Sr) using a Thermo Fisher iCAP 7400 radial Inductively Coupled Plasma Optical Emission Spectrometer (ICP-OES). Samples and calibration standards were internally standardized by using 1 mg L^{-1} Y and Lu. The analytical precision for these elements is better than 3‰.

4. Results

4.1. Sulfur isotopes

Data from both sections record a gradual positive sulfur-isotope excursion (SIE) with a magnitude of ∼20‰ and final maximum values of ∼40‰ (Fig. 2), agreeing well with that reported from the Yunjia section (∼500 m away from Wölong) described by Newton et al. (2011). In the Nianduo section, with a well-constrained T-OAE *n*CIE, the positive SIE begins around −8 m stratigraphically below the onset level of the T-OAE *n*CIE at −2 m. Recently, foraminiferal and chemostratigraphic constraints allow the interval at the top of the Pupuga Formation to be referred to as the uppermost Pliensbachian to lowermost Toarcian (Han et al., 2018, 2021). Consequently, the SIE onset (Wölong: −3 m and Nianduo: −8 m), which corresponds to a small negative CIE in $\delta^{13}C_{TOC}$ at Nianduo (∼ −12 to −5 m), may be assigned to around the Pl–To boundary.

Pre-SIE $\delta^{34}S_{CAS}$ values mainly vary between 16.8 to 23.0‰, with an average of ∼19.8‰ for the Nianduo section (∼ −28.6 to −10.6 m; Fig. 2), figures that are relatively close to those in the same interval (∼ −36.4 to −4.2 m) of the Wölong section (Han et al., 2022a), with a range and average of 17.7 to 23.0‰ and 20.9‰, respectively. A positive excursion of ∼20‰ is observed in both sections, and the highest values are attained approximately at the end of the recovery interval of the T-OAE *n*CIE, leveling off with a range and average, respectively, of 33.6 to 41.8‰ and 39.8‰ for Nianduo (∼23.4 to 45.4 m) and of 38.5 to 43.9‰ and 41.9‰ for Wölong (∼20.9 to 29.9 m).

4.2. Elemental concentration

The whole-rock $CaCO_3$ concentrations mainly range from 75% to 95%, with an average value of ∼88.0% for the Nianduo section and

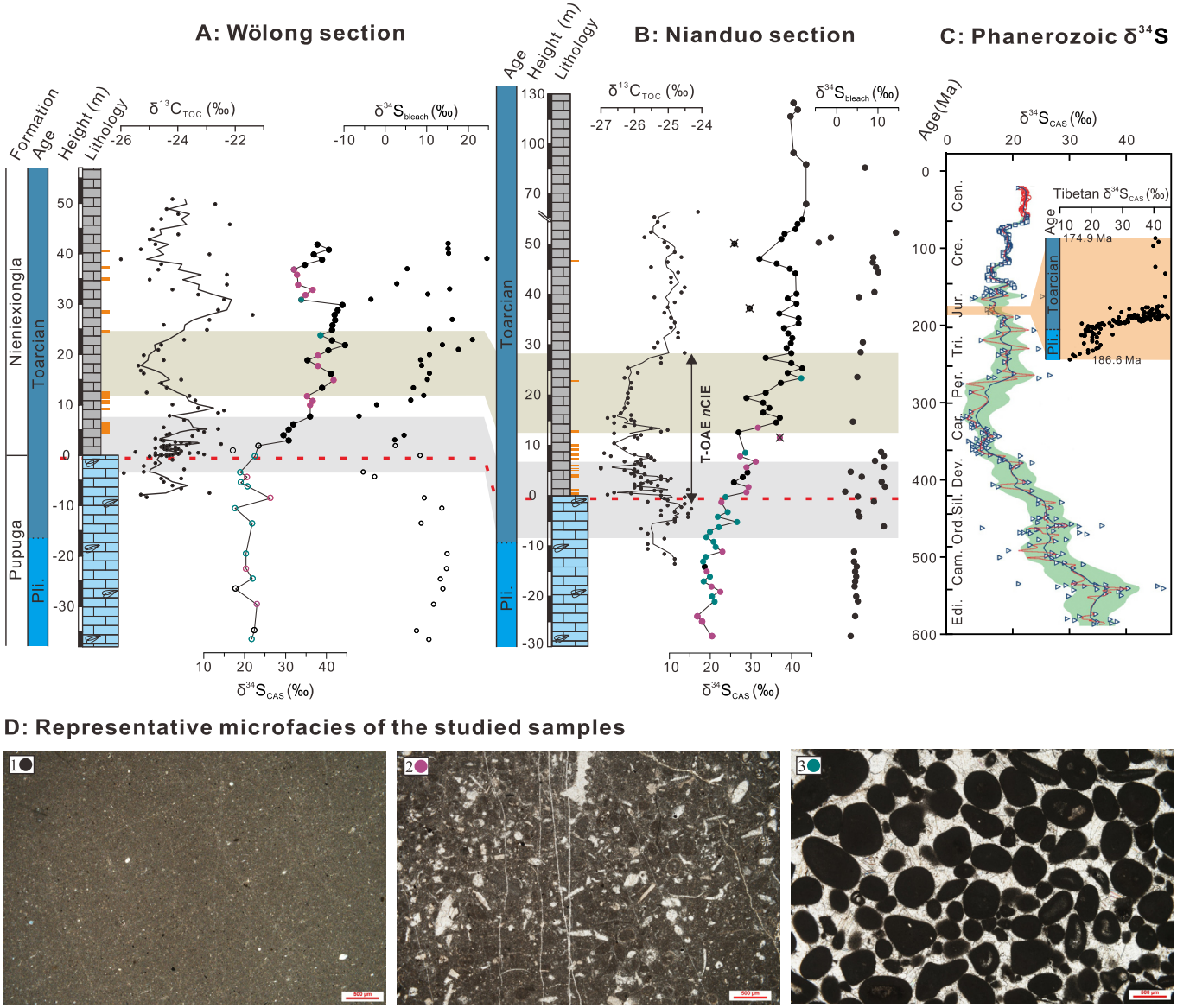

Fig. 2. Chemostratigraphy of the upper Pliensbachian–Toarcian interval from the Wölong (**A**) and Nianduo (**B**) sections, and Phanerozoic seawater sulfate $\delta^{34}S$ (**C**), superimposed upon the late Pliensbachian–Toarcian $\delta^{34}S$ data of Tibet (brown zone). The black lines through the $\delta^{13}C_{TOC}$ data are 3-point moving average values from the Nianduo and Wölong sections, excluding the data points identified as non-primary (Han et al., 2018). $\delta^{34}S_{CAS}$ and $\delta^{34}S_{bleach}$ data (hollow circles) of the lower Wölong section are from Han et al. (2022a). Note that each unit scale bar below and above ~55 m of the Nianduo section represents 5 and 15 m, respectively. The two horizontal bars correlate the two major Toarcian positive phases. Compiled Phanerozoic $\delta^{34}S$ data are from Algeo et al. (2015) and Tibetan data from Han et al. (2022a) and this study (Figs. 2 and 3). Sulfur isotopes of Tibet are illustrated with representative microfacies (**D**): 1 (black data points): Mudstone; 2 (purple data points): Wackestone/Packstone; 3 (blue data points): Grainstone.

of ~90.1% for the Wölong section (Fig. 3). The CAS sulfur content in both sections is relatively low, ranging from 3 to 40 ppm with an average of ~14.8 ppm. Carbonate Mg/Ca and Mn/Sr ratios range predominantly between 0.005 to 0.01 and 0.05 to 0.4, respectively.

5. Discussion

5.1. Preservation and diagenetic evaluation of $\delta^{34}S_{CAS}$

The sulfur-isotope ratio of structurally incorporated carbonate-associated sulfate (CAS) in the carbonate lattice is commonly considered to record the coeval isotopic composition of global seawater sulfate, if not modified by diagenetic processes (Gill et al., 2008; Fike et al., 2015) and/or experimental contamination during the CAS extraction (Marenco et al., 2008; Wotte et al., 2012). In this study, thorough NaOCl bleach and consecutive NaCl rinses have been applied to remove non-CAS sulfur, and steps have been taken to minimize the possibility of reduced-sulfur oxidation during the acid dissolution of the carbonate (see section 3.1). The results show that the $\delta^{34}S_{CAS}$ of all samples displays much higher values than that of paired $\delta^{34}S_{bleach}$ (Fig. 2A–B), and there was no or only weak correlation observed between the two parameters in Nianduo and Wölong, respectively (Fig. 3A). Furthermore, all the analyzed samples were checked under the microscope and visible pyrite was only present in very minor quantities. Hence, reduced-sulfur phases should have been largely removed during the NaOCl bleaching, and the $\delta^{34}S_{CAS}$ values are not likely to have been influenced by the oxidation of residual sulfide minerals during CAS extraction. Only one data point (50.4 m, Nianduo section) has both low $\delta^{34}S_{bleach}$ and $\delta^{34}S_{CAS}$ values compared to stratigraphically adjacent samples and might have suffered contamination due to oxidation of reduced-sulfur compounds during CAS extraction.

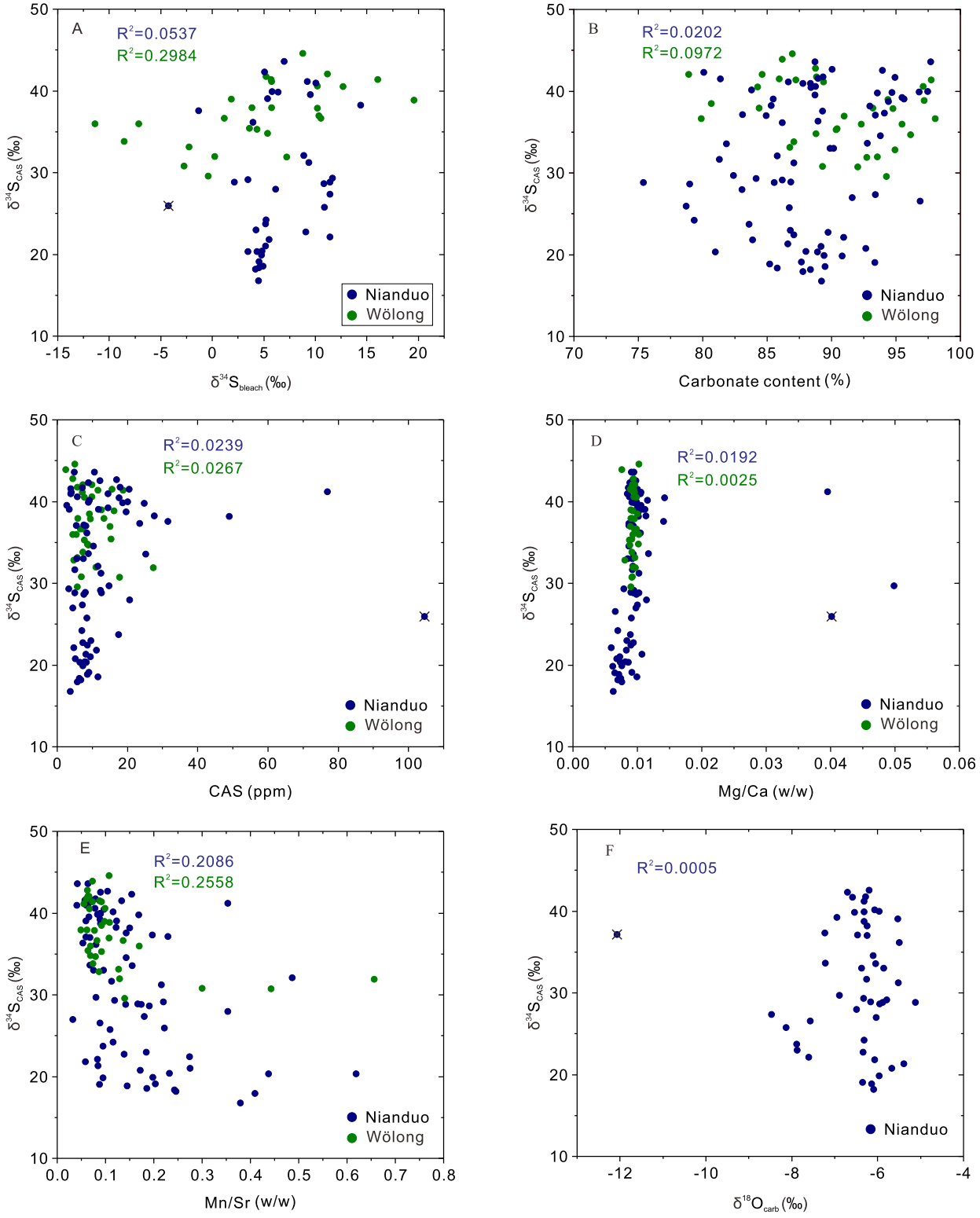

Fig. 3. Cross-plots of carbonate isotopic values and elemental concentration for Nianduo (blue) and Wölong (green) sections. (**A**) $\delta^{34}S_{CAS}$ (‰)-$\delta^{34}S_{bleach}$ (‰) (R^2 = 0.0537 and 0.2984), (**B**) $\delta^{34}S_{CAS}$ (‰)-Carbonate content (%) (R^2 = 0.0202 and 0.0972), (**C**) $\delta^{34}S_{CAS}$ (‰)-[CAS] (ppm) (R^2 = 0.0239 and 0.0267), (**D**) $\delta^{34}S_{CAS}$ (‰)-Mg/Ca (w/w) (R^2 = 0.0192 and 0.0025), (**E**)$\delta^{34}S_{CAS}$ (‰)-Mn/Sr (w/w) (R^2 = 0.2086 and 0.2558), (**F**) $\delta^{34}S_{CAS}$ (‰)-$\delta^{18}O_{carb}$ (‰) (R^2 = 0.0005, $\delta^{18}O_{carb}$ data from Han et al. (2018).

Different carbonate components (micrite, sparite and fossils) and different depositional conditions can lead to large variability in $\delta^{34}S_{CAS}$ (Present et al., 2015; Richardson et al., 2019; Rose et al., 2019). No correlation is observed between $\delta^{34}S_{CAS}$ and HCl-leachable carbonate content in the Tibetan sections (Fig. 3B). Furthermore, petrographic analyses of the studied samples show three characteristic microfacies types, each with a wide range of $\delta^{34}S_{CAS}$ values (Fig. 2A–B and D). In both sections, the proportion of micrite is overall similar throughout the Nieniexiongla Formation, while this interval shows a significant rise in $\delta^{34}S_{CAS}$. Notably, the intergranular pores of grainstones in the upper Pupuga Formation are filled with sparite (Han et al., 2016), which is generally considered to be secondary. However, the circumgranular cement rims (sparite) of carbonate grains (microfacies 3) generally suggest a marine-phreatic and marine vadose environments (Han et al., 2016) and thus could still record a seawater signal. This supposition is supported by the fact that $\delta^{34}S_{CAS}$ datapoints from microfacies 3 characterized by sparry cements do not show unique values compared to adjacent datapoints with different microfacies. Combined, these observations suggest that facies had negligible influence on $\delta^{34}S_{CAS}$ across the studied archives. Additionally, dolomitization and diagenetic alteration can alter $\delta^{34}S_{CAS}$ (Gill et al., 2008; Present et al., 2015; Fichtner et al., 2017). In this study, $\delta^{34}S_{CAS}$ data show no correlation with Mg/Ca (as proxy for dolomitization), and [CAS], Mn/Sr and $\delta^{18}O_{carb}$ (proxies for diagenesis) (Fig. 3C–F). Furthermore, no visible dolomitic samples have been observed under the microscope in the Pl–To interval (Han et al., 2016). Importantly, the high-resolution $\delta^{34}S_{CAS}$ trends from the two Tibetan sections are very similar and the trend of gradually increasing values corresponds well to those from Europe, albeit with a significant difference in magnitude (Fig. 4; Gill et al., 2011a; Newton et al., 2011). Consequently, the $\delta^{34}S_{CAS}$ of the studied samples are taken to record primary sulfur isotopic values for at least (supra)regional seawater sulfate.

Only two individual data points at 10.4 m and 37.4 m of the Nianduo section have lower $\delta^{34}S_{CAS}$ values compared to stratigraphically adjacent samples (Fig. 2B), with corresponding abnormal $\delta^{18}O_{carb}$ and Mg/Ca values (Fig. 2A and F), respectively, pointing to probable diagenetic alteration and/or dolomitization. Therefore, these two data points are omitted from data interpretation in addition to the sample (50.4 m, Nianduo section), excluded because of potential transfer from the reduced-sulfur pool as discussed above.

5.2. Amplified sulfur-isotope spatial heterogeneity

Because the Tethyan shallow-water carbonate platforms locally can lack characteristic Lower Jurassic carbon-isotope excursions (e.g., Trecalli et al., 2012; Han et al., 2018; Ettinger et al., 2021), we additionally use the $\delta^{34}S_{CAS}$ records combined with biostratigraphy, carbon isotopes, facies change and *Lithiotis* extinction for correlation. The Nianduo and Yorkshire correlating with carbon isotopes and biostratigraphy means that the $\delta^{34}S$ excursion in both places happened at the same time. Although the Wölong section does not have the characteristic *n*CIEs during the Pl–To boundary and early Toarcian intervals (Han et al., 2018), the similar $\delta^{34}S$ records and relatively close distance with the Nianduo section allow the direct correlation combined with the facies change and *Lithiotis* extinction. The correlation with Monte Sorgenza is less certain, but the facies change, *Lithiotis* extinction and the onset of the T-OAE *n*CIE could act as useful markers. Notably, the Nianduo section has a well-defined and globally comparable T-OAE *n*CIE in organic carbon and higher resolution $\delta^{34}S$ data, and is hence used as the primary reference for the Tibetan record. The onset of the positive SIE in Tibetan sections occurs around the Pl–To boundary, thus preceding the onset of the T-OAE *n*CIE, as is also observed in Yorkshire, UK (Fig. 4; Gill et al., 2011a; Newton et al., 2011). However, in the platform carbonates of the southern Apennines (Italy), the onset of the SIE and T-OAE *n*CIE appears to be almost synchronous, possibly an artefact of the relatively low-resolution $\delta^{34}S$ data or minor local erosive modification. Although the increasing trends are comparable globally, the positive SIE magnitude (~20‰ in Tibet versus ~5‰ in Europe) during the T-OAE, as well as post-T-OAE values (~40‰ in Tibet versus ~22‰ in Europe) are significantly different. The Tibetan $\delta^{34}S$ positive excursion originally observed by Newton et al. (2011) was suggested to represent a modified geochemical signal due to a major difference in the magnitude shift in $\delta^{34}S_{CAS}$ relative to the European realm (Gill et al., 2011a). However, multiple proxies and the reproducibility of the signal across the two sections studied here indicate that the high-resolution $\delta^{34}S_{CAS}$ data of Tibet likely represent a primary seawater signal. Consequently, the observed and amplified spatial heterogeneity in marine Toarcian sulfur isotopes questioned by Gill et al. (2011a) is here confirmed as genuine.

Importantly, high $\delta^{34}S_{CAS}$ values (~40‰) as observed for the post-SIE in the Tibetan sections have previously only been observed for the Late Proterozoic and Cambrian (Fig. 2C; e.g., Kampschulte and Strauss, 2004; Gill et al., 2011b). Although the Tibetan $\delta^{34}S_{CAS}$ values could theoretically have derived from extremely restricted settings related to the presence of geographic barriers that resulted in a unique $\delta^{34}S_{CAS}$ evolution during the Toarcian in this region, such hypothesis is not supported by the regional palaeogeography. The Jurassic Tibetan Himalaya was located in a relatively narrow linear zone on the northern Indian margin, with the studied area directly connected to the open Tethys Ocean. The close affinity of bivalve and foraminiferal species between the Tibetan Himalaya and western Tethys (Han et al., 2021) and similar absolute $\delta^{34}S_{CAS}$ values during the pre-T-OAE interval (Han et al., 2022a) suggest that water masses were relatively well mixed before the event, thereby excluding the existence of such major geographical barriers. Additionally, evidence for significant global sea-level rise and enhanced storm activity likely characterized the entire tropic/subtropic Tethys in the early Toarcian (Hallam, 1981; Krencker et al., 2015; Han et al., 2018). Such conditions would have favored improved watermass exchanges compared to earlier times. Alternatively, and possibly more likely, extremely low seawater sulfate concentrations (0.6–5 mM), due to widespread evaporite and pyrite burial during the Early Jurassic, have been suggested as the cause for such distinct spatial differences in sulfur-isotope ratios in seawater across early Toarcian ocean basins (Newton et al., 2011; Xu et al., 2018b; Han et al., 2022a and references therein). When global seawater sulfate concentrations fall to a level such that the seawater sulfate residence time is shorter than or equal to global average oceanic mixing time, $\delta^{34}S$ records are more prone to being affected by local/regional processes, and thus are also more likely to show different values and trends between geographically separated ocean basins (Newton et al., 2011; Han et al., 2022a).

5.3. Modeling the Toarcian sulfur cycle

The large-magnitude positive SIE of the early Toarcian was interpreted as representing a global increase in pyrite burial under geographically expanded anoxic/euxinic oceanic conditions (Gill et al., 2011a; Newton et al., 2011). Such conditions could have been favorable for microbially mediated organic-matter remineralization, sulfate reduction and pyrite burial. Increasingly, studies have indicated that the burial of sulfurized organic matter could have played a significant role in carbon and sulfur burial and thus had important feedbacks for the carbon cycle, although to date these studies have focused on the Cenomanian–Turonian oceanic anoxic event (OAE 2) (e.g., Hülse et al., 2019; Raven et al., 2019). It is possible that organic-sulfur burial was also an important process

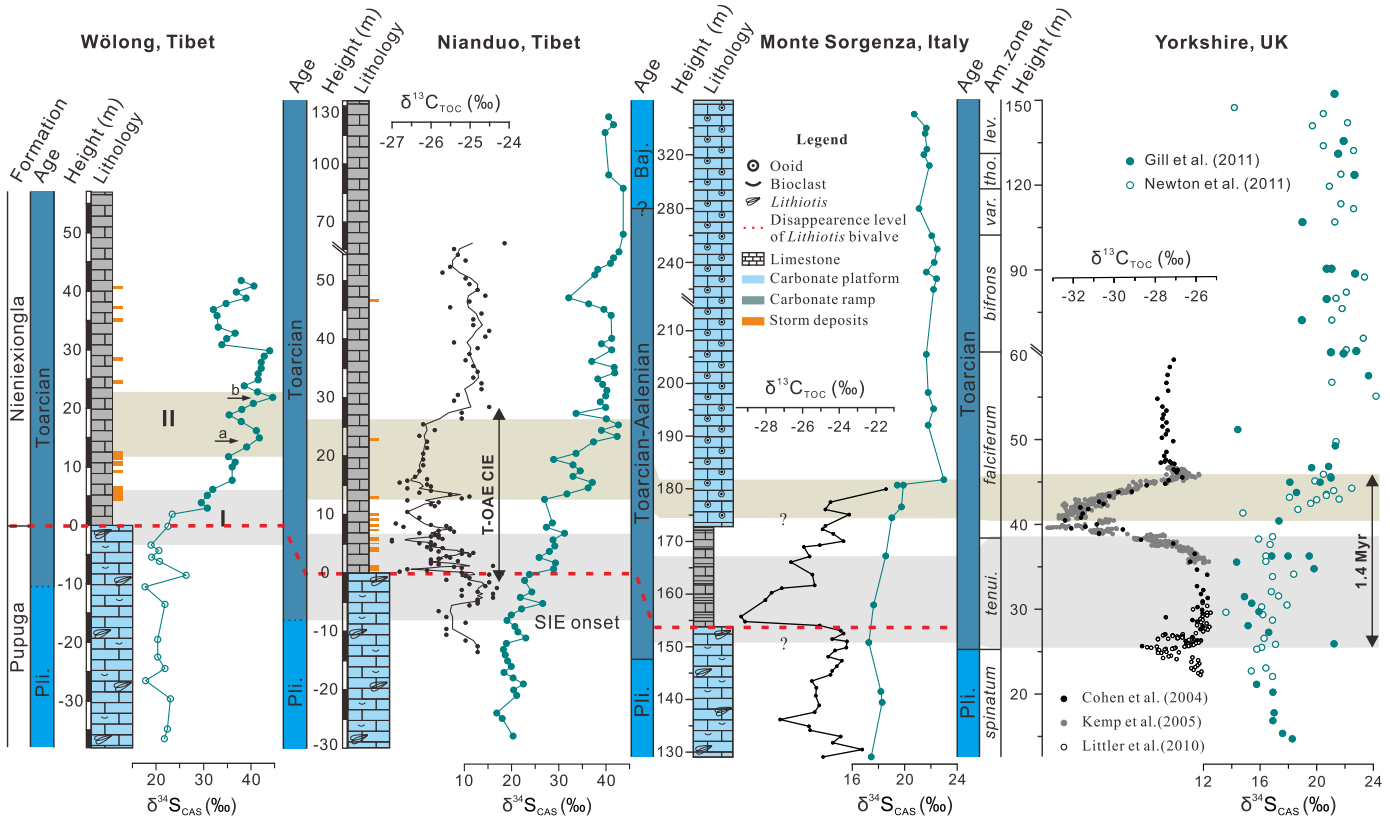

Fig. 4. Global chemostratigraphic correlation of $\delta^{13}C$ and $\delta^{34}S_{CAS}$ during the Pliensbachian–Toarcian interval. The correlation is based on the onset, end and phase of the positive sulfur-isotope excursion. Isotope data of Monte Sorgenza (Italy) are from Gill et al. (2011a) and Newton et al. (2011), and of Yorkshire (UK) from Cohen et al. (2004); Kemp et al. (2005); Littler et al. (2010); Gill et al. (2011a) and Newton et al. (2011). The red dashed line illustrates the abrupt boundary between bioclastic grainstones (below) and deeper water micrites (upper) and also the disappearance of the Lithiotis Fauna. Note: (1) The $\delta^{13}C_{TOC}$ data of Monte Sorgenza are used for chemostratigraphy, rather than $\delta^{13}C_{carb}$ data, because the onset of the T-OAE CIE identified from $\delta^{13}C_{TOC}$ data broadly corresponds well with the disappearance of reef-building *Lithiotis*, as observed in other Tethyan carbonate platforms; (2) The change in the *y-axis* scale in the Nianduo, Monte Sorgenza and Yorkshire plots at 55, 215 and 60 m, respectively is due to a reduction in sampling resolution.

during the early Toarcian, although this idea remains to be tested as records of organic-sulfur burial are currently lacking. Both pyrite and organic sulfur are relatively enriched in ^{32}S, so the effect of enhanced reduced-sulfur burial of either of these geochemical species during the early Toarcian would have driven seawater $\delta^{34}S$ to more positive values. The rising limb of the SIE is estimated to be ~1.4–1.5 Myr in duration (Fig. 5; see Supplementary material), thereby indicating long-term global oceanic deoxygenation and an enhanced reduced-sulfur burial flux beginning around the Pl–To boundary and continuing throughout the early Toarcian. Given the sulfur-isotope heterogeneity of the oceans during the Toarcian confirmed by the data in this study, there is an inherent difficulty in determining a quantitative global picture of the sulfur cycle from any single isotope record. Here, application of a sulfur-cycle box model (see Supplementary material) based on that used in Witts et al. (2018) can reproduce the signals seen in Tibet or Europe using a pulse of increased reduced-sulfur burial of between 2–4 times that of the background fluxes during the SIE interval, and with sulfate concentrations of between 1 and 5 mM, respectively (see Supplementary material; Fig. S1).

Notably, such a model, with consistently high seawater sulfate concentration values, fails to reproduce the extended period (likely ~8 Myr until the end-Toarcian; see Supplementary material; Fig. S1) of observed, prolonged positive $\delta^{34}S_{seawater}$ values after the T-OAE both in Tibet and Europe. Whilst the absolute $\delta^{34}S$ values differ between Tibet and Europe, this long mid-late Toarcian plateau is a persistent feature of both sulfur-isotope records. Maintaining a globally high reduced-sulfur burial flux throughout this period could theoretically have resulted in this feature and there may be some support for this from Tl isotopes that suggest that anoxia (and therefore enhanced reduced-sulfur burial) persisted into the middle Toarcian (Fig. 6; Them et al., 2018). However, organic-carbon isotopes in a stratigraphically expanded succession from the Mochras borehole in Wales (UK), and other time-equivalent successions, suggest that enhanced organic-carbon burial did not persist beyond the middle Toarcian (Fig. 1A; e.g., Xu et al., 2018b).

To closely reproduce prolonged positive $\delta^{34}S_{seawater}$ values in sulfur cycle box-model simulations, without invoking persistently elevated reduced-sulfur burial requires rather specific conditions, with the proportion of marine sulfate buried globally as Ca-sulfate (gypsum plus anhydrite) at very low values. This scenario can be achieved if seawater sulfate and/or calcium concentrations are lowered to such an extent that it is difficult for evaporation to concentrate seawater past the Ca-sulfate saturation point. A near cessation of global Ca-sulfate deposition during the T-OAE would have forced an increase in the relative proportion of total reduced sulfur, because these two major burial pathways were coupled, and mutually regulated. Such a mechanism would have allowed the absolute amount of reduced-sulfur burial to fall after the T-OAE *n*CIE, whilst maintaining a positive plateau in the seawater sulfate-$\delta^{34}S$ composition, which would be maintained as long as sulfate concentrations remained below the Ca-sulfate precipitation threshold. A similar mechanism has been proposed for the carbon-isotope system, where a decreased carbonate weathering flux to the ocean can result in higher proportional organic-carbon burial, and a long-term change to more positive carbonate-$\delta^{13}C$ compositions (Shields and Mills, 2017). This scenario is broadly consistent with wider evidence of reduced seawater sulfate concentrations

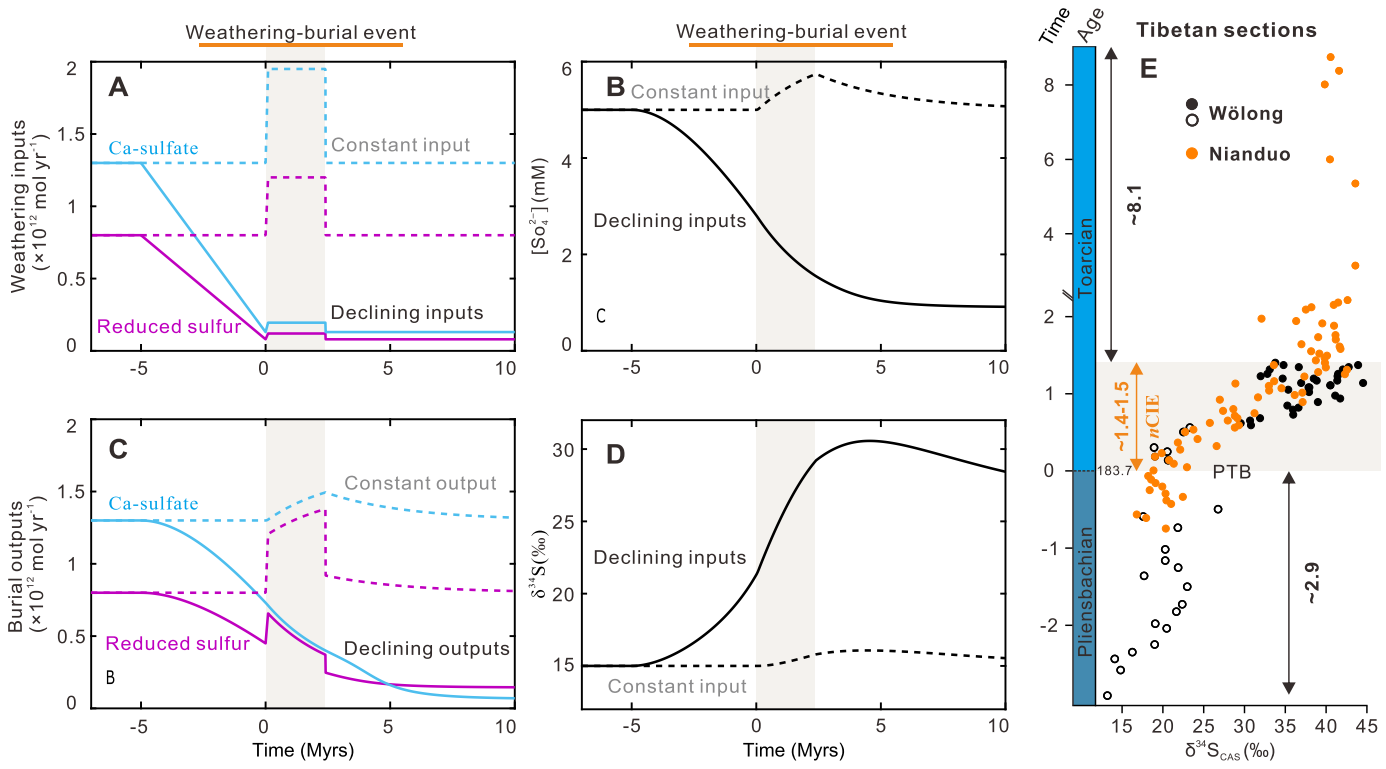

Fig. 5. Long-term sulfur-cycle model for the late Pliensbachian to Toarcian interval. Panels show changes in weathering inputs of Ca-sulfate and reduced sulfur. (**A**), seawater $[SO_4^{2-}]$ (**B**), and paired burial outputs (**C**) and seawater $\delta^{34}S$ (**D**). Dashed lines show default model where weathering inputs of sulfur do not change, and solid lines show model where weathering inputs decrease and $[SO_4^{2-}]$ drops below the Ca-sulfate deposition threshold, causing a rise in $\delta^{34}S$. Panel E shows the Tibetan $\delta^{34}S$ data calibrated against the numerical time scale that is determined in the Supplementary material; PTB: Pl–To boundary (~183.7 Ma).

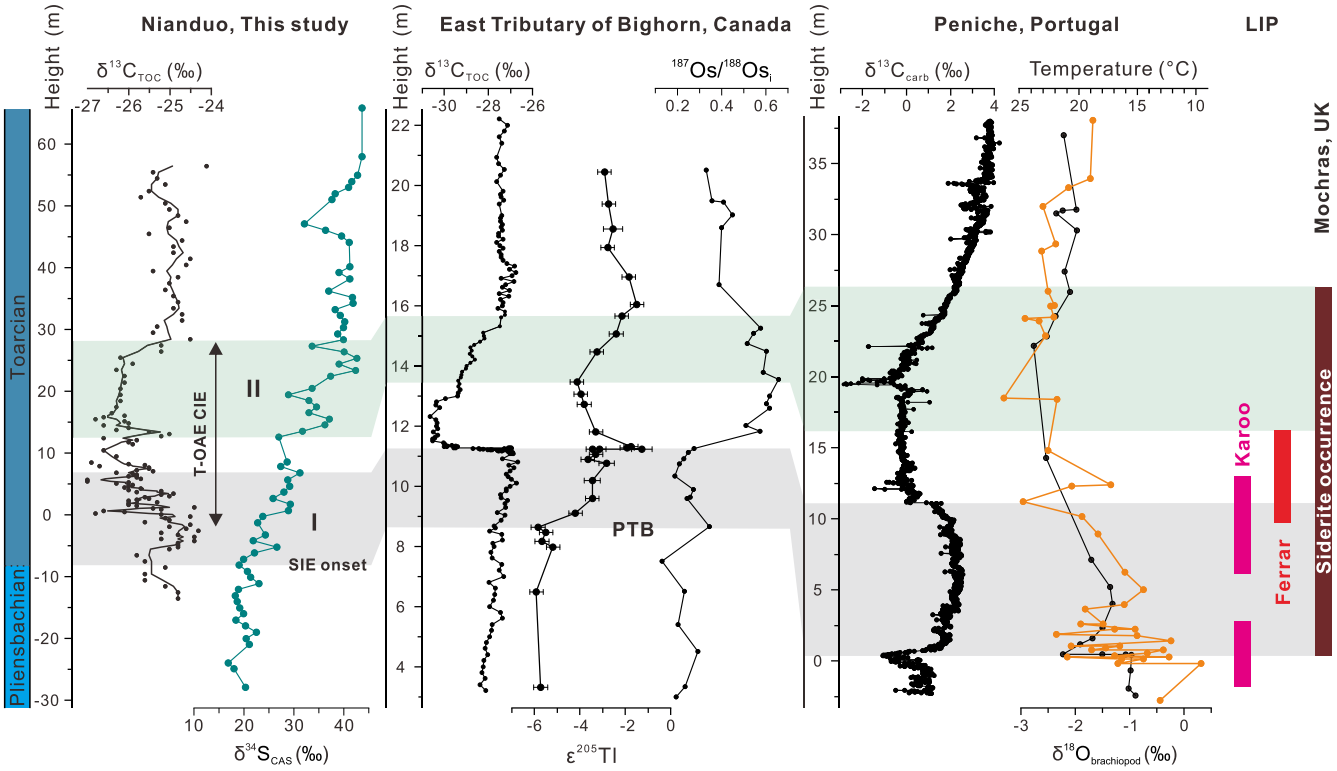

Fig. 6. Multiple early Toarcian geochemical records illustrating the relationship between different environmental perturbations. For Nianduo (Tibet), $\delta^{13}C_{TOC}$ data are from Han et al. (2018); For East Tributary of Bighorn (Canada), $\delta^{13}C_{TOC}$ data are from Them II et al. (2017), $\varepsilon^{205}Tl$ data (ocean deoxygenation) from Them et al. (2018) and $^{187}Os/^{188}Os$ data (continental weathering) from Them et al. (2017); For Peniche (Portugal), $\delta^{13}C_{carb}$ data are from Hesselbo et al. (2007) and $\delta^{13}O$ data (sea-surface temperature) of brachiopods from Suan et al. (2008) and Müller et al. (2020); For Karoo-Ferrar LIP (Large Igneous Province) activity data are from Burgess et al. (2015); Percival et al. (2015); Xu et al. (2018a) and Al-Suwaidi et al. (2022); For Mochras (UK), the stratigraphic position of siderite occurrence is from Xu et al. (2018b). SIE: sulfur-isotope excursion.

across the event: the T-OAE has been linked to low ocean sulfate via the rate of change in the CAS-isotope record and by the appearance of abundant siderite in some European sections (Fig. 6), geochemical patterns that coincide with, and in some instances start earlier than the *n*CIE interval (Gill et al., 2011a; Newton et al., 2011; Xu et al., 2018b; Han et al., 2022a). Importantly, there is evidence of extensive evaporite deposition in the proto-Atlantic during the Late Triassic to Early Jurassic (Turner and Sherif, 2007), which provides a mechanism of significant sulfate drawdown prior to the T-OAE.

To test this hypothesis, we first modified the model of Witts et al. (2018) by adding a logistic function, which curtails reduced-sulfur burial when marine sulfate concentrations approach zero, to prevent sulfate concentrations becoming negative. We furthermore impose a rule on the model that Ca-sulfate deposition stops at seawater sulfate concentrations of 1 mM. This threshold is chosen arbitrarily to represent the point at which Ca-sulfate deposition in evaporite systems becomes negligible. In Fig. S2 of Supplementary material, we experiment with changing this value. Further work modeling the 3D distribution of Early Jurassic seawater chemistry would be necessary to define this more precisely but is outside the scope of this study as the qualitative mechanism we wish to demonstrate does not depend on the quantities chosen. We assume that seawater sulfate in the run-up to the T-OAE has been significantly lowered by declining weathering fluxes of both reduced-sulfur and Ca-sulfate (Fig. 5A–B). Reduced continental weathering is consistent with the records of long-term strontium-isotope decline from the Late Triassic onwards (Jones et al., 1994; McArthur et al., 2020), a Phanerozoic low point in clastic sediment deposition in the Early Jurassic (Hay et al., 2006), and colder late Pliensbachian temperatures well before the onset of the SIE (Korte et al., 2015). Additionally, the long-term enhanced deposition of evaporite sulfate during the Late Triassic–Early Jurassic (Turner and Sherif, 2007) would have hastened the decrease of sulfate concentrations towards the Ca-sulfate precipitation threshold during the Toarcian.

A greatly reduced ocean sulfate reservoir and depressed Ca-sulfate burial flux in the early Toarcian implies that a much smaller amount of reduced-sulfur burial is required than previously modeled to generate the observed range of increases in $\delta^{34}S$ (Fig. 5C–E). Furthermore, altering the threshold in our model at which Ca-sulfate burial becomes negligible can alter the $\delta^{34}S$ value at which the system plateaus (Fig. S2). It is worth noting that the enhanced reduced-sulfur flux needed to drive the system below the Ca-sulfate deposition threshold is small relative to modern fluxes ($\sim$0.8x10^{12} mol yr^{-1} vs 1.9x10^{12} mol yr^{-1}; Bottrell and Newton, 2006) because of the much smaller size of the early Toarcian sulfate reservoir and so does not require any enhancement of the reactive iron flux to the oceans. Such a scenario may indeed better match the likely scale of marine anoxia needed to explain the more limited nature of the biotic response (Sepkoski, 1982). Whilst the absolute value for seawater sulfate that controls the Ca-sulfate deposition threshold remains to be more accurately determined, the proposed mechanism also strongly suggests that the sulfate concentration during the T-OAE was at the lower end of previous estimates. This result is consistent with evidence of enhanced siderite deposition from Mochras (UK) during the *tenuicostatum* and *exaratum* subzones of the early Toarcian (Fig. 6; Xu et al., 2018b) and decreases the upper limit of reduced-sulfur fluxes needed to create either the European or Tibetan seawater $\delta^{34}S$ response. Whilst siderite could theoretically be the result of TOC limitation, this is not the case for this interval of the Mochras core (average TOC of 1.05 wt%), suggesting that low seawater sulfate, which limits reduced-sulfur production during the mineralization of organic matter, favored the reaction of dissolved iron and carbonate ions during early diagenesis (Xu et al., 2018b and references therein).

5.4. Stepwise ocean deoxygenation and its termination

The high-resolution $\delta^{34}S$ data and extended T-OAE CIE interval ($\sim$30 m) of the Tibetan sections (primarily referring to Nianduo, as mentioned above), allow us to explore the deoxygenation processes through time. There are two significant phases (I and II) in the observed overall SIE towards exceptionally heavy isotopic values in the eastern Tethys (Fig. 4). The first begins around the Pl–To boundary and ends at the decreasing limb of the T-OAE *n*CIE, and the second starts at the increasing limb and finally culminates at the end of the *n*CIE. These observations suggest that ocean deoxygenation and the accompanying increase in reduced-sulfur burial were triggered before the traditionally defined T-OAE starting at the mid-*tenuicostatum* Zone of the earliest Toarcian (Fig. 1A; Jenkyns et al., 2002; Xu et al., 2018a) and overall experienced two major phases. This pattern is broadly consistent with the two shifts to higher $\varepsilon^{205}Tl$ in the East Tributary of the Bighorn section in Canada (Fig. 6; Them et al., 2018). Additionally, the $\delta^{34}S$ data of Nianduo allow us to infer a geologically synchronous coupling between deoxygenation and carbon-cycle evolution. Phase I correlates closely with an interval characterized by a negative CIE around the Pl–To boundary extending to the onset level of the T-OAE *n*CIE that was recorded globally and interpreted as being driven by the release of isotopically light carbon associated with the onset of Karoo-Ferrar LIP activity (Fig. 6; Hesselbo et al., 2000; Kemp et al., 2005; Burgess et al., 2015; Percival et al., 2015; Ruhl et al., 2022). The coupled sulfur- and carbon-isotope systems in this interval broadly correspond with the idea of elevated weathering rates and seawater temperature indicated by $^{187}Os/^{188}O_S$ and $\delta^{18}O$ from belemnites and brachiopods respectively (Fig. 6; Suan et al., 2008; Korte et al., 2015; Müller et al., 2020). Thus, the deoxygenation of phase I may have been mediated by transient global warming reducing the solubility of oceanic oxygen and/or weathering-driven enhanced primary production by increased fluvially derived nutrients, and an associated elevated organic-carbon flux to the seabed, consuming oxygen and creating an expanded oxygen minimum zone. The ensuing phase II may have had the similar causes as deoxygenation in phase I, because of the overall correspondence with the positive and negative plateau values of $^{187}Os/^{188}Os$ and $\delta^{18}O$, respectively.

The Tibetan $\delta^{34}S_{CAS}$ record reaches peak values around the end of the rising limb of the T-OAE *n*CIE, consistent with those observed from European records (Fig. 4). These observations suggest that the termination of ocean deoxygenation and associated reduced-sulfur burial was broadly synchronous with the end of globally enhanced organic-carbon burial rates. Additionally, the termination of the increasing trend in $\delta^{34}S$ also marks the point at which the sulfur cycle reaches a new steady state with a negligible Ca-sulfate deposition flux driving an increase in the proportion of the total sulfur flux from the ocean deposited as reduced sulfur, thereby maintaining the long-term elevated seawater $\delta^{34}S$ values (Fig. 5).

5.5. Drivers of high Tibetan $\delta^{34}S_{CAS}$ and spatial heterogeneity

The Tibetan SIE starts in shallow-water platform carbonates (~ -10 to 0 m; Fig. 2), which are dominated by grainstones including lumps, oncoids and ooids with abundant benthic fauna, suggesting relatively turbulent oxygenated waters (Han et al., 2016, 2021). Although the ensuing SIE (>0 m in the sections) is encoded in deeper water ramp facies that developed due to sea-level rise during the T-OAE, the TOC level is rather low ($\sim$0.1%wt; (Newton

et al., 2011; Han et al., 2018). Additionally, in the southern Apennines (Italy), the SIE also starts in oolitic and bioclastic grainstones, continues in clay-rich carbonates, and ends in oolitic grainstones (Gill et al., 2011a). These observations suggest that the positive SIE of the Kioto and southern Apennine Platforms, respectively on the eastern and western Tethyan continental margins, did not initiate in anoxic/euxinic conditions and was therefore not driven by *in situ* enhanced reduced-sulfur burial. The SIE observed in these two sites was therefore more likely to have been affected in different ways by (supra)regional factors under conditions of extremely low sulfate concentrations.

Notably, appreciable TOC and reduced-sulfur burial have been observed in several far-traveled thrust slices of the Panthalassan sea floor (Japan and eastern Russia), which represent the deep-sea sediments (principally made up of radiolarian cherts) deposited below the calcite compensation depth (Fig. 1C; Gröcke et al., 2011; Ikeda et al., 2018; Filatova et al., 2022). In a recent study of a deep peri-equatorial Panthalassan site, TOC values, trace elements, iron-speciation data and sulfur isotopes in pyrite suggest anoxic/euxinic conditions across an interval from the Pl–To boundary to the T-OAE (Chen et al., 2022, 2023; Kemp et al., 2022b). Substantial discrete increases in organic matter and pyrite concentration at the Pl–To boundary and during the T-OAE *n*CIE suggest enhanced deep ocean burial of sulfur and carbon at these times (Chen et al., 2022, 2023; Kemp et al., 2022b). Additionally, positive $\delta^{34}S_{pyrite}$ excursions with magnitudes of > 10‰ were observed in these two key intervals. These excursions were interpreted as due to enhanced organic-carbon supply and/or preservation on the seafloor that fueled bacterial sulfate reduction (BSR), causing the positive sulfur-isotope shift in pyrite (Chen et al., 2022). These two intervals of positive $\delta^{34}S_{pyrite}$ shift broadly correspond to the positive phase I and II of $\delta^{34}S_{CAS}$ (Fig. 4), respectively. In the Early Jurassic, these deep-sea localities were at low latitudes between 10°N and 10°S based on palaeomagnetic and palaeontological data (Ando et al., 2001), although the number of studies is rather limited because Lower Jurassic oceanic crust, and thus the open-ocean pelagic cover, has largely been subducted. The classical Cretaceous OAEs in the early Aptian (OAE1a) and at the Cenomanian–Turonian boundary (OAE2) do have an impressive black-shale record across the deep-sea floor of low-latitude zones of Panthalassa (Jenkyns, 2010). Therefore, a major deep-water carbon and reduced-sulfur sink during the T-OAE may have similarly developed in low-latitude zones of high organic productivity, which were close to the site of the Tibetan sections located in the open southeastern Tethys (Fig. 1C). The much higher Tibetan $\delta^{34}S$ values are thus inferred to have been related to upwelling and mixing of ^{34}S-enriched low-latitude deep waters that were affected by open-ocean reduced-sulfur burial adjacent to the Tethys Himalaya.

The pattern of enhanced reduced-sulfur burial in low-latitude deep-sea settings could also reasonably explain the apparent discrepancy in absolute $\delta^{34}S_{CAS}$ values during the syn- and post-T-OAE intervals between Tibet and Europe. The north European shelf-sea basins recording the T-OAE were locally stratified and restricted, as indicated by biomarkers and multiple geochemical proxies (e.g., McArthur et al., 2008; Dickson et al., 2017). The rise in $\delta^{34}S_{CAS}$ started abruptly, well after the rise in TOC, sedimentary pyrite concentrations and total sulfur content seen in sections from the European shelf-sea basins (Jenkyns and Clayton, 1997; Newton et al., 2011; Xu et al., 2018b), suggesting that local anoxia/euxinia and associated enhanced reduced- sulfur burial could have driven this SIE. Therefore, a uniform magnitude for the positive SIE would be expected only in local watermasses of the European shelf basins. However, this is not the case for the similarly sized positive SIE present in the better ventilated southern Apennines that was situated on the western Tethyan continental margin (Gill et al., 2011a). This similar geochemical response in varied European settings could have been caused by the much larger reduced-sulfur burial sink in the low-latitude zones that may have dwarfed the same process elsewhere.

6. Conclusions and implications

Two $\delta^{34}S_{CAS}$ profiles reported from the Tibetan Himalaya of the southeastern Tethys show similar signatures and their increasing trend parallels those previously documented in Toarcian sediments from the western Tethys and northern Europe. However, the positive SIE (with a magnitude of ~20‰ in Tibet versus ~5‰ in Europe) beginning around the Pl–To boundary and culminating around the end of the T-OAE *n*CIE interval, and persistent post-T-OAE positive $\delta^{34}S$ values (~40‰ in Tibet versus ~22‰ in Europe), are significantly different, which confirms a spatially heterogeneous ocean with respect to seawater $\delta^{34}S$ at that time. A long-term sulfur-cycle box model suggests that: (1) The persistent post-*n*CIE positive $\delta^{34}S$ was likely maintained by a long-term downwards shift in the relative proportion of oxidized (Ca-sulfate) to reduced sulfur (pyrite and organic sulfur) burial; (2) A shift to negligible Ca-sulfate precipitation was likely driven by the forcing of global seawater to low sulfate conditions caused by a long-term decline in the weathering flux to the oceans and massive burial of evaporite sulfate throughout the Late Triassic and Early Jurassic, followed by enhanced reduced-sulfur burial associated with Toarcian anoxia.

The Tibetan high-resolution and stratigraphically extended $\delta^{34}S_{CAS}$ data reveal two major phases of ocean deoxygenation in the early Toarcian. The first began around the Pl–To boundary and continued up to the onset of the T-OAE *n*CIE, whilst the second began at the recovery phase and terminated around the end of the T-OAE *n*CIE. The termination of deoxygenation also marks the point where the sulfur cycle reached a new steady state with a negligible Ca-sulfate burial flux. The upwelling of ^{34}S-enriched deep water, affected by reduced-sulfur burial could have caused the greatly amplified SIE in Tibet, which at that time was directly adjacent to the equatorial zones, whereas the dampened magnitude in Europe could be attributed to a smaller local reduced-sulfur sink.

The links between low sulfate, Ca-sulfate burial and the maintenance of elevated seawater sulfate-$\delta^{34}S$ established in this study may well apply to other time periods with similar sulfur-isotope records. Further work to establish links between the major ion composition of seawater and the rate of Ca-sulfate deposition should allow an independent approach to estimating seawater sulfate during times when seawater sulfate is low and there is evidence of its isotopic heterogeneity. Observed heterogeneity in seawater sulfate-$\delta^{34}S$ poses challenges for estimating global reduced-sulfur burial fluxes and the extent of oceanic anoxia. However, such constraints will improve insights into links between the global carbon and sulfur cycles, and global temperature evolution during LIP-induced warming events.

CRediT authorship contribution statement

Zhong Han: Conceptualization, Data curation, Funding acquisition, Investigation, Writing – original draft, Visualization. **Xiumian Hu:** Conceptualization, Funding acquisition, Project administration, Supervision, Writing – review & editing. **Robert J. Newton:** Conceptualization, Writing – original draft, Writing – review & editing, Funding acquisition. **Tianchen He:** Methodology, Writing – review & editing. **Benjamin J.W. Mills:** Visualization, Writing – review & editing. **Hugh C. Jenkyns:** Writing – review & editing. **Micha Ruhl:** Writing – review & editing. **Robert A. Jamieson:** Data curation.

Declaration of competing interest

The authors declare that they have no known competing financial interests or personal relationships that could have appeared to influence the work reported in this paper.

Data availability

The data supporting the finding of this study are available from corresponding author upon reasonable request.

Acknowledgements

We thank the support of staff and students of the Cohen Geochemistry Laboratories at University of Leeds, for their technical and analytical support. This work is funded by the National Natural Science Foundation of China (NSFC; Grant Nos. 42002121, 41888101 and 42272116), a scholarship grant from China Scholarship Council (201706190163), and a research grant (2021-LAMD-K03) from the State Key Laboratory of Mineral Deposit Research of Nanjing University. R.J.N. and T.C.H were financially supported by the Natural Environment Research Council (NERC; Grant No NE/N018559/1). This manuscript is a contribution to IGCP 739 project: *The Mesozoic–Palaeogene hyperthermal events* and to Integrated Understanding of the Early Jurassic Earth System and Timescale (JET) project.

Appendix A. Supplementary material

Supplementary material related to this article can be found online at https://doi.org/10.1016/j.epsl.2023.118404.

References

Al-Suwaidi, A.H., Ruhl, M., Jenkyns, H.C., Damborenea, S.E., Manceñido, M.O., Condon, D.J., Angelozzi, G.N., Kamo, S.L., Storm, M., Riccardi, A.C., Hesselbo, S.P., 2022. New age constraints on the Lower Jurassic Pliensbachian–Toarcian Boundary at Chacay Melehue (Neuquén Basin, Argentina). Sci. Rep. 12, 4975.

Algeo, T.J., Luo, G.M., Song, H.Y., Lyons, T.W., Canfield, D.E., 2015. Reconstruction of secular variation in seawater sulfate concentrations. Biogeosciences 12, 2131–2151.

Ando, A., Kodama, K., Kojima, S., 2001. Low-latitude and Southern Hemisphere origin of Anisian (Triassic) bedded chert in the Inuyama area, Mino terrane, central Japan. J. Geophys. Res., Solid Earth 106, 1973–1986.

Bottrell, S.H., Newton, R.J., 2006. Reconstruction of changes in global sulfur cycling from marine sulfate isotopes. Earth-Sci. Rev. 75, 59–83.

Burgess, S.D., Bowring, S.A., Fleming, T.H., Elliot, D.H., 2015. High-precision geochronology links the Ferrar large igneous province with early-Jurassic ocean anoxia and biotic crisis. Earth Planet. Sci. Lett. 415, 90–99.

Caruthers, A.H., Grocke, D.R., Smith, P.L., 2011. The significance of an Early Jurassic (Toarcian) carbon-isotope excursion in Haida Gwaii (Queen Charlotte Islands), British Columbia, Canada. Earth Planet. Sci. Lett. 307, 19–26.

Chen, W., Kemp, D.B., He, T., Newton, R.J., Xiong, Y., Jenkyns, H.C., Izumi, K., Cho, T., Huang, C., Poulton, S.W., 2023. Shallow- and deep-ocean Fe cycling and redox evolution across the Pliensbachian–Toarcian boundary and Toarcian Oceanic Anoxic Event in Panthalassa. Earth Planet. Sci. Lett. 602, 117959.

Chen, W., Kemp, D.B., Newton, R.J., He, T., Huang, C., Cho, T., Izumi, K., 2022. Major sulfur cycle perturbations in the Panthalassic Ocean across the Pliensbachian-Toarcian boundary and the Toarcian Oceanic Anoxic Event. Glob. Planet. Change 215, 103884.

Cohen, A.S., Coe, A.L., Harding, S.M., Schwark, L., 2004. Osmium isotope evidence for the regulation of atmospheric CO_2 by continental weathering. Geology 32, 157–160.

Dickson, A.J., Gill, B.C., Ruhl, M., Jenkyns, H.C., Porcelli, D., Idiz, E., Lyons, T.W., van den Boorn, S.H.J.M., 2017. Molybdenum-isotope chemostratigraphy and paleoceanography of the Toarcian Oceanic Anoxic Event (Early Jurassic). Paleoceanography 32, 813–829.

Ettinger, N.P., Larson, T.E., Kerans, C., Thibodeau, A.M., Hattori, K.E., Kacur, S.M., Martindale, R.C., 2021. Ocean acidification and photic-zone anoxia at the Toarcian Oceanic Anoxic Event: insights from the Adriatic Carbonate Platform. Sedimentology 68, 63–107.

Fantasia, A., Föllmi, K.B., Adatte, T., Bernárdez, E., Spangenberg, J.E., Mattioli, E., 2018. The Toarcian Oceanic Anoxic Event in southwestern Gondwana: an example from the Andean Basin, northern Chile. J. Geol. Soc. (Lond.) 175, 883–902.

Fichtner, V., Strauss, H., Immenhauser, A., Buhl, D., Neuser, R.D., Niedermayr, A., 2017. Diagenesis of carbonate associated sulfate. Chem. Geol. 463, 61–75.

Fike, D.A., Bradley, A.S., Rose, C.V., 2015. Rethinking the ancient sulfur cycle. Annu. Rev. Earth Planet. Sci. 43, 593–622.

Filatova, N.I., Konstantinovskaya, E., Vishnevskaya, V., 2022. Jurassic-Lower Cretaceous siliceous rocks and black shales from allochthonous complexes of the Koryak-Western Kamchatka orogenic belt, East Asia. Int. Geol. Rev. 64, 311–330.

Garrels, R.M., Lerman, A., 1981. Phanerozoic cycles of sedimentary carbon and sulfur. Proc. Natl. Acad. Sci. 78, 4652–4656.

Gill, B.C., Lyons, T.W., Frank, T.D., 2008. Behavior of carbonate-associated sulfate during meteoric diagenesis and implications for the sulfur isotope paleoproxy. Geochim. Cosmochim. Acta 72, 4699–4711.

Gill, B.C., Lyons, T.W., Jenkyns, H.C., 2011a. A global perturbation to the sulfur cycle during the Toarcian Oceanic Anoxic Event. Earth Planet. Sci. Lett. 312, 484–496.

Gill, B.C., Lyons, T.W., Young, S.A., Kump, L.R., Knoll, A.H., Saltzman, M.R., 2011b. Geochemical evidence for widespread euxinia in the Later Cambrian ocean. Nature 469, 80–83.

Gröcke, D.R., Hori, R.S., Trabucho-Alexandre, J., Kemp, D.B., Schwark, L., 2011. An open ocean record of the Toarcian oceanic anoxic event. Solid Earth 2, 245–257.

Hallam, A., 1981. A revised sea-level curve for the early Jurassic. J. Geol. Soc. (Lond.) 138, 735–743.

Han, Z., Hu, X., BouDagher-Fadel, M., Jenkyns, H.C., Franceschi, M., 2021. Early Jurassic carbon-isotope perturbations in a shallow water succession from the Tethys Himalaya, southern hemisphere. Newsl. Stratigr. 54, 461–481.

Han, Z., Hu, X., He, T., Newton, R.J., Jenkyns, H.C., Jamieson, R.A., Franceschi, M., 2022a. Early Jurassic long-term oceanic sulfur-cycle perturbations in the Tibetan Himalaya. Earth Planet. Sci. Lett. 578, 117261.

Han, Z., Hu, X., Hu, Z., Jenkyns, H.C., Su, T., 2022b. Geochemical evidence from the Kioto Carbonate Platform (Tibet) reveals enhanced terrigenous input and deoxygenation during the early Toarcian. Glob. Planet. Change 215, 103887.

Han, Z., Hu, X., Kemp, D.B., Li, J., 2018. Carbonate-platform response to the Toarcian Oceanic Anoxic Event in the southern hemisphere: implications for climatic change and biotic platform demise. Earth Planet. Sci. Lett. 489, 59–71.

Han, Z., Hu, X., Li, J., Garzanti, E., 2016. Jurassic carbonate microfacies and relative sea-level changes in the Tethys Himalaya (southern Tibet). Palaeogeogr. Palaeoclimatol. Palaeoecol. 456, 1–20.

Hay, W.W., Migdisov, A., Balukhovsky, A.N., Wold, C.N., Flögel, S., Söding, E., 2006. Evaporites and the salinity of the ocean during the Phanerozoic: implications for climate, ocean circulation and life. Palaeogeogr. Palaeoclimatol. Palaeoecol. 240, 3–46.

He, T., Zhu, M., Mills, B.J.W., Wynn, P.M., Zhuravlev, A.Y., Tostevin, R., Pogge von Strandmann, P.A.E., Yang, A., Poulton, S.W., Shields, G.A., 2019. Possible links between extreme oxygen perturbations and the Cambrian radiation of animals. Nat. Geosci. 12, 468–474.

Hesselbo, S.P., Gröcke, D.R., Jenkyns, H.C., Bjerrum, C.J., Farrimond, P., Morgans Bell, H.S., Green, O.R., 2000. Massive dissociation of gas hydrate during a Jurassic oceanic anoxic event. Nature 406, 392–395.

Hesselbo, S.P., Jenkyns, H.C., Duarte, L.V., Oliveira, L.C.V., 2007. Carbon-isotope record of the Early Jurassic (Toarcian) Oceanic Anoxic Event from fossil wood and marine carbonate (Lusitanian Basin, Portugal). Earth Planet. Sci. Lett. 253, 455–470.

Hu, X., Li, J., Han, Z., Li, Y., 2020. Two types of hyperthermal events in the Mesozoic–Cenozoic: environmental impacts, biotic effects, and driving mechanisms. Sci. China Earth Sci. 63, 1–18.

Hu, X., Wang, J., Boudagher-Fadel, M., Garzanti, E., An, W., 2016. New insights into the timing of the India – Asia collision from the Paleogene Quxia and Jialazi formations of the Xigaze forearc basin, South Tibet. Gondwana Res. 32, 76–92.

Huang, W.T., van Hinsbergen, D.J., Dekkers, M.J., Garzanti, E., Dupont-Nivet, G., Lippert, P.C., Li, X.C., Maffione, M., Langereis, C.G., Hu, X.M., 2015. Paleolatitudes of the Tibetan Himalaya from primary and secondary magnetizations of Jurassic to Lower Cretaceous sedimentary rocks. Geochem. Geophys. Geosyst. 16, 77–100.

Hülse, D., Arndt, S., Ridgwell, A., 2019. Mitigation of extreme ocean anoxic event conditions by organic matter sulfurization. Paleoceanogr. Paleoclimatol. 34, 476–489.

Ikeda, M., Hori, R.S., Ikehara, M., Miyashita, R., Chino, M., Yamada, K., 2018. Carbon cycle dynamics linked with Karoo-Ferrar volcanism and astronomical cycles during Pliensbachian-Toarcian (Early Jurassic). Glob. Planet. Change 170, 163–171.

Jadoul, F., Berra, F., Garzanti, E., 1998. The Tethys Himalayan passive margin from Late Triassic to Early Cretaceous (South Tibet). J. Asian Earth Sci. 16, 173–194.

Jenkyns, H.C., 1988. The early Toarcian (Jurassic) anoxic event; stratigraphic, sedimentary and geochemical evidence. Am. J. Sci. 288, 101–151.

Jenkyns, H.C., 2010. Geochemistry of oceanic anoxic events. Geochem. Geophys. Geosyst. 11, Q03004.

Jenkyns, H.C., Clayton, C.J., 1986. Black shales and carbon isotopes in pelagic sediments from the Tethyan Lower Jurassic. Sedimentology 33, 87–106.

Jenkyns, H.C., Clayton, C.J., 1997. Lower Jurassic epicontinental carbonates and mudstones from England and Wales: chemostratigraphic signals and the early Toarcian anoxic event. Sedimentology 44, 687–706.

Jenkyns, H.C., Jones, C.E., Grocke, D.R., Hesselbo, S.P., Parkinson, D.N., 2002. Chemostratigraphy of the Jurassic System: applications, limitations and implications for palaeoceanography. J. Geol. Soc. (Lond.) 159, 351–378.

Jones, C.E., Jenkyns, H.C., Hesselbo, S.P., 1994. Strontium isotopes in Early Jurassic seawater. Geochim. Cosmochim. Acta 58, 1285–1301.
Kampschulte, A., Strauss, H., 2004. The sulfur isotopic evolution of Phanerozoic seawater based on the analysis of structurally substituted sulfate in carbonates. Chem. Geol. 204, 255–286.
Kemp, D.B., Suan, G., Fantasia, A., Jin, S., Chen, W., 2022a. Global organic carbon burial during the Toarcian oceanic anoxic event: patterns and controls. Earth-Sci. Rev. 231, 104086.
Kemp, D.B., Chen, W., Cho, T., Algeo, T.J., Shen, J., Ikeda, M., 2022b. Deep-ocean anoxia across the Pliensbachian-Toarcian boundary and the Toarcian Oceanic Anoxic Event in the Panthalassic Ocean. Glob. Planet. Change 212, 103782.
Kemp, D.B., Coe, A.L., Cohen, A.S., Schwark, L., 2005. Astronomical pacing of methane release in the Early Jurassic period. Nature 437, 396–399.
Kemp, D.B., Selby, D., Izumi, K., 2020. Direct coupling between carbon release and weathering during the Toarcian oceanic anoxic event. Geology 48, 976–980.
Korte, C., Hesselbo, S.P., Ullmann, C.V., Dietl, G., Ruhl, M., Schweigert, G., Thibault, N., 2015. Jurassic climate mode governed by ocean gateway. Nat. Commun. 6, 10015.
Krencker, F.N., Bodin, S., Suan, G., Heimhofer, U., Kabiri, L., Immenhauser, A., 2015. Toarcian extreme warmth led to tropical cyclone intensification. Earth Planet. Sci. Lett. 425, 120–130.
Littler, K., Hesselbo, S.P., Jenkyns, H.C., 2010. A carbon-isotope perturbation at the Pliensbachian-Toarcian boundary: evidence from the Lias Group, NE England. Geol. Mag. 147, 181–192.
Liu, G.H., Einsele, G., 1994. Sedimentary history of the Tethyan basin in the Tibetan Himalayas. Geol. Rundsch. 83, 32–61.
Marenco, P.J., Corsetti, F.A., Hammond, D.E., Kaufman, A.J., Bottjer, D.J., 2008. Oxidation of pyrite during extraction of carbonate associated sulfate. Chem. Geol. 247, 124–132.
McArthur, J.M., Algeo, T.J., van de Schootbrugge, B., Li, Q., Howarth, R.J., 2008. Basinal restriction, black shales, Re-Os dating, and the Early Toarcian (Jurassic) oceanic anoxic event. Paleoceanography 23, PA4217.
McArthur, J.M., Howarth, R.J., Shields, G.A., Zhou, Y., 2020. Chapter 7 - Strontium isotope stratigraphy. In: Gradstein, F.M., Ogg, J.G., Schmitz, M.D., Ogg, G.M. (Eds.), Geologic Time Scale 2020. Elsevier, pp. 211–238.
Müller, T., Jurikova, H., Gutjahr, M., Tomašových, A., Schlögl, J., Liebetrau, V., Duarte, L.v., Milovský, R., Suan, G., Mattioli, E., Pittet, B., Eisenhauer, A., 2020. Ocean acidification during the early Toarcian extinction event: evidence from boron isotopes in brachiopods. Geology 48, 1184–1188.
Newton, R.J., Reeves, E.P., Kafousia, N., Wignall, P.B., Bottrell, S.H., Sha, J.-G., 2011. Low marine sulfate concentrations and the isolation of the European epicontinental sea during the Early Jurassic. Geology 39, 7–10.
Percival, L.M., Cohen, A.S., Davies, M.K., Dickson, A.J., Hesselbo, S.P., Jenkyns, H.C., Leng, M.J., Mather, T.A., Storm, M.S., Xu, W., 2016. Osmium isotope evidence for two pulses of increased continental weathering linked to Early Jurassic volcanism and climate change. Geology 44, 759–762.
Percival, L.M.E., Witt, M.L.I., Mather, T.A., Hermoso, M., Jenkyns, H.C., Hesselbo, S.P., Al-Suwaidi, A.H., Storm, M.S., Xu, W., Ruhl, M., 2015. Globally enhanced Mercury deposition during the end-Pliensbachian extinction and Toarcian OAE: a link to the Karoo-Ferrar Large Igneous Province. Earth Planet. Sci. Lett. 428, 267–280.
Present, T.M., Paris, G., Burke, A., Fischer, W.W., Adkins, J.F., 2015. Large Carbonate Associated Sulfate isotopic variability between brachiopods, micrite, and other sedimentary components in Late Ordovician strata. Earth Planet. Sci. Lett. 432, 187–198.
Raven, M.R., Fike, D.A., Bradley, A.S., Gomes, M.L., Owens, J.D., Webb, S.A., 2019. Paired organic matter and pyrite δ34S records reveal mechanisms of carbon, sulfur, and iron cycle disruption during Ocean Anoxic Event 2. Earth Planet. Sci. Lett. 512, 27–38.
Richardson, J.A., Keating, C., Lepland, A., Hints, O., Bradley, A.S., Fike, D.A., 2019. Silurian records of carbon and sulfur cycling from Estonia: the importance of depositional environment on isotopic trends. Earth Planet. Sci. Lett. 512, 71–82.
Rose, C.V., Webb, S.M., Newville, M., Lanzirotti, A., Richardson, J.A., Tosca, N.J., Catalano, J.G., Bradley, A.S., Fike, D.A., 2019. Insights into past ocean proxies from micron-scale mapping of sulfur species in carbonates. Geology 47, 833–837.
Ruhl, M., Hesselbo, S.P., Jenkyns, H.C., Xu, W., Silva, R.L., Matthews, K.J., Mather, T.A., Mac Niocaill, C., Riding, J.B., 2022. Reduced plate motion controlled timing of Early Jurassic Karoo-Ferrar large igneous province volcanism. Sci. Adv. 8, eabo0866.
Scotese, C.R., 2021. An atlas of Phanerozoic paleogeographic maps: the seas come in and the seas go out. Annu. Rev. Earth Planet. Sci. 49, 679–728.
Sepkoski, J.J., 1982. A Compendium of Fossil Marine Families. Contributions to Biology and Geology. Milwaukee Public Museum, p. 155.
Shields, G.A., Mills, B.J.W., 2017. Tectonic controls on the long-term carbon isotope mass balance. Proc. Natl. Acad. Sci. 114, 4318–4323.
Silva, R.L., Duarte, L.V., Wach, G.D., Ruhl, M., Sadki, D., Gómez, J.J., Hesselbo, S.P., Xu, W., O'Connor, D., Rodrigues, B., Filho, J.G.M., 2021. An Early Jurassic (Sinemurian–Toarcian) stratigraphic framework for the occurrence of Organic Matter Preservation Intervals (OMPIs). Earth-Sci. Rev. 221, 103780.
Suan, G., Mattioli, E., Pittet, B., Mailliot, S., Lecuyer, C., 2008. Evidence for major environmental perturbation prior to and during the Toarcian (Early Jurassic) oceanic anoxic event from the Lusitanian Basin, Portugal. Paleoceanography 23, PA001459.
Them II, T., Gill, B., Caruthers, A., Gröcke, D., Tulsky, E., Martindale, R., Poulton, T., Smith, P., 2017. High-resolution carbon isotope records of the Toarcian Oceanic Anoxic Event (Early Jurassic) from North America and implications for the global drivers of the Toarcian carbon cycle. Earth Planet. Sci. Lett. 459, 118–126.
Them, T.R., Gill, B.C., Caruthers, A.H., Gerhardt, A.M., Gröcke, D.R., Lyons, T.W., Marroquín, S.M., Nielsen, S.G., Trabucho Alexandre, J.P., Owens, J.D., 2018. Thallium isotopes reveal protracted anoxia during the Toarcian (Early Jurassic) associated with volcanism, carbon burial, and mass extinction. Proc. Natl. Acad. Sci. 115, 6596–6601.
Them, T.R., Gill, B.C., Selby, D., Gröcke, D.R., Friedman, R.M., Owens, J.D., 2017. Evidence for rapid weathering response to climatic warming during the Toarcian Oceanic Anoxic Event. Sci. Rep. 7, 5003.
Trecalli, A., Spangenberg, J., Adatte, T., Follmi, K.B., Parente, M., 2012. Carbonate platform evidence of ocean acidification at the onset of the early Toarcian oceanic anoxic event. Earth Planet. Sci. Lett. 357, 214–225.
Turner, P., Sherif, H., 2007. A giant Late Triassic–Early Jurassic evaporitic basin on the Saharan Platform, North Africa. J. Geol. Soc. (Lond.) 285, 87–105.
Witts, J.D., Newton, R.J., Mills, B.J., Wignall, P.B., Bottrell, S.H., Hall, J.L., Francis, J.E., Crame, J.A., 2018. The impact of the Cretaceous–Paleogene (K–Pg) mass extinction event on the global sulfur cycle: evidence from Seymour Island, Antarctica. Geochim. Cosmochim. Acta 230, 17–45.
Wotte, T., Shields-Zhou, G.A., Strauss, H., 2012. Carbonate-associated sulfate: experimental comparisons of common extraction methods and recommendations toward a standard analytical protocol. Chem. Geol. 326, 132–144.
Xu, W., Mac Niocaill, C., Ruhl, M., Jenkyns, H.C., Riding, J.B., Hesselbo, S.P., 2018a. Magnetostratigraphy of the Toarcian Stage (Lower Jurassic) of the Llanbedr (Mochras Farm) Borehole, Wales: basis for a global standard and implications for volcanic forcing of palaeoenvironmental change. J. Geol. Soc. (Lond.) 175, 594–604.
Xu, W., Ruhl, M., Jenkyns, H.C., Leng, M.J., Huggett, J.M., Minisini, D., Ullmann, C.V., Riding, J.B., Weijers, J.W., Storm, M.S., 2018b. Evolution of the Toarcian (Early Jurassic) carbon-cycle and global climatic controls on local sedimentary processes (Cardigan Bay Basin, UK). Earth Planet. Sci. Lett. 484, 396–411.